Close-up view of an ongoing merger between the NGC 4839 group and the Coma cluster – a post-merger scenario

N. Lyskova [1,2,3,4]★ E. Churazov,[2,4] C. Zhang [4] W. Forman,[5] C. Jones,[5] K. Dolag,[4,6] E. Roediger[7] and A. Sheardown[7]

[1]*National Research University Higher School of Economics, Myasnitskaya str 20, Moscow 101000, Russia*
[2]*Space Research Institute (IKI), Profsoyuznaya 84/32, Moscow 117997, Russia*
[3]*ASC of P.N.Lebedev Physical Institute, Leninskiy prospect 53, Moscow 119991, Russia*
[4]*Max-Planck-Institut für Astrophysik, Karl-Schwarzschild-Strasse 1, D-85741 Garching, Germany*
[5]*Harvard-Smithsonian Center for Astrophysics, 60 Garden Street, Cambridge, MA 02138, USA*
[6]*University Observatory Munich, Scheinerstr 1, D-81679 Munich, Germany*
[7]*E.A. Milne Centre for Astrophysics, School of Mathematics and Physical Sciences, University of Hull, Hull HU6 7RX, UK*

ABSTRACT

We study a merger of the NGC 4839 group with the Coma cluster using X-ray observations from the *XMM–Newton* and *Chandra* telescopes. X-ray data show two prominent features: (i) a long (∼600 kpc in projection) and bent tail of cool gas trailing (towards south-west) the optical centre of NGC 4839, and (ii) a 'sheath' region of enhanced X-ray surface brightness enveloping the group, which is due to hotter gas. While at first glance the X-ray images suggest that we are witnessing the first infall of NGC 4839 into the Coma cluster core, we argue that a post-merger scenario provides a better explanation of the observed features and illustrate this with a series of numerical simulations. In this scenario, the tail is formed when the group, initially moving to the south-west, reverses its radial velocity after crossing the apocenter, the ram pressure ceases and the ram pressure-displaced gas falls back towards the centre of the group and overshoots it. Shortly after the apocenter passage, the optical galaxy, dark matter, and gaseous core move in a north-east direction, while the displaced gas continues moving to the south-west. The 'sheath' is explained as being due to interaction of the re-infalling group with its own tail of stripped gas mixed with the Coma gas. In this scenario, the shock, driven by the group before reaching the apocenter, has already detached from the group and would be located close to the famous relic to the south-west of the Coma cluster.

Key words: X-rays: individual: Coma cluster, NGC 4839 – X-rays: galaxies: clusters.

1 INTRODUCTION

According to the current cosmological concordance model, galaxy clusters form hierarchically through a combination of rare major merger events and more gentle continuous accretion of smaller groups of galaxies throughout cosmic time along filamentary structures (e.g. Kravtsov & Borgani 2012; Vikhlinin et al. 2014). The latter actually represents the dominant channel of galaxy cluster growth in mass and in the number of member galaxies (see e.g. Berrier et al. 2009; Dolag et al. 2009; Genel et al. 2010). The best sites for studying structure formation processes are the galaxy cluster outskirts, which represent the transition region between the virialized intracluster medium (ICM) approximately in hydrostatic equilibrium, and the infalling material from the surroundings.

Mergers and accretion events often leave imprints on the distribution of the hot ICM such as shocks, cold fronts, and ram pressure stripped tails which could be observed with X-ray observations (e.g. Sun et al. 2006, 2010; Markevitch & Vikhlinin 2007; Su et al. 2017, among others). In particular, the appearance of extended tails of ram pressure stripped gas provides valuable information for recovering the 3D geometry of a merger event, the orbital stage of a subhalo (early infall, pre-/post-pericenter passage), and even ICM plasma properties such as viscosity, magnetic fields, thermal conduction (Roediger et al. 2015a,b, among others). Structure formation processes in galaxy clusters can be studied with radio observations of radio relics, which are believed to trace large-scale shock waves generated by a merger or accretion, (e.g. Ensslin et al. 1998; van Weeren et al. 2009; Di Gennaro et al. 2018).

The Coma cluster of galaxies (Abell 1656), the third brightest X-ray cluster, is one of the nearest and best-studied galaxy clusters. Optical and X-ray observations have revealed a wealth of

★ E-mail: lyskova@mpa-garching.mpg.de

substructure in the Coma cluster (Colless & Dunn 1996; Vikhlinin, Forman & Jones 1997; Briel et al. 2001; Neumann et al. 2003; Adami et al. 2005; Andrade-Santos et al. 2013, among others). One of the most prominent is the group of galaxies associated with the elliptical galaxy NGC 4839. It lies in the cluster outskirts (∼1 Mpc in projection) south-west of the cluster centre. The X-ray image (see Fig. 1) exhibits an edge-like structure at the head of the group and an elongated tail of ram pressure stripped gas towards the south-west, i.e. opposite to the direction to the Coma centre. The NGC 4839 group appears to be merging with the Coma cluster core, and the tail direction is approximately aligned with a filament connecting the Coma cluster with Abell 1367, which, in turn, is part of the 'Great Wall' (e.g. Geller & Huchra 1989; Neumann et al. 2001; Brown & Rudnick 2011). It has long been debated whether observations are consistent with a simple radial infall or imply a tangential orbit (Biviano et al. 1996), and whether we observe the first passage (Colless & Dunn 1996; Neumann et al. 2001; Akamatsu et al. 2013, among others) or the group has already passed the Coma cluster centre (Burns et al. 1994).

Based on galaxy redshifts, Colless & Dunn (1996) constrained the 3D geometry of the Coma-NGC 4839 merger using a simple dynamical two-body model, in which the two clusters were considered as point masses following a linear orbit under their mutual gravity. They estimated that the angle between merging objects and the observer is most likely to be $\alpha = 74°^{+5}_{-10}$, i.e. the merger happens almost in the plane of the sky, the true 3D separation is 0.8 ± 0.1 h^{-1} Mpc and the infall velocity is 1700^{+350}_{-500} km s^{-1}. Colless & Dunn (1996) argued that the NGC 4839 group is just beginning to penetrate the Coma cluster.

Coma, as a typical merging cluster, also hosts a radio halo and a relic. The Coma radio relic is located ∼2.1 Mpc in projection from the cluster centre, beyond the NGC 4839 group, but in the same south-west direction. Based on radio and optical observations, Brown & Rudnick (2011) suggested that the Coma radio relic is due to an infall shock, caused by the infall of a 'wall' of galaxies possibly associated with NGC 4839 into the Coma cluster. However, large radio relics (radio gischt), in general, are believed to be associated with outgoing merger shocks (e.g. Bonafede et al. 2009; van Weeren et al. 2010, among others). Analyses of *XMM–Newton* (Ogrean & Brüggen 2013) and *Suzaku* observations (Akamatsu et al. 2013) revealed a tentative temperature discontinuity across the Coma relic, which has been interpreted as a shock front with a Mach number of $M \sim 2$. Moreover, a tentative detection of a pressure jump at the position of the radio relic has been reported (Erler et al. 2015) based on the thermal Sunyaev–Zel'dovich effect data extracted from the first public all-sky data release of *Planck*.

Based on a weak gravitational lensing survey performed with the Subaru/Suprime-Cam, Okabe et al. (2014) detected a subhalo associated with the NGC 4839 group and measured its mass to be $\sim 10^{13}$ M$_\odot$, assuming a Navarro–Frenk–White (NFW) profile with a truncation radius of ∼100 kpc. Curiously, the X-ray peak derived from the *XMM–Newton* image is spatially coincident with the NGC 4839 elliptical galaxy, but both are shifted ≃ 1 arcmin ≃ 30 kpc towards the west from the weak-lensing mass centre (see fig. 2b in Sasaki et al. 2016).

Here, we analyse available *XMM–Newton* and *Chandra* observations. To constrain the 3D geometry and a trajectory of the infalling group, we compare the X-ray maps with smoothed-particle hydrodynamic (SPH) simulations. In Sections 2 and 3 we describe general X-ray properties of the Coma cluster and the NGC 4839 group, respectively. The simulation set-up is outlined in Section 4, followed by a discussion of pre-merger and post-merger scenarios

in Section 5. We discuss the mass and gas temperature of the NGC 4839 group in Section 6 and summarize our findings in Section 7.

All our results are scaled to a flat ΛCDM cosmology with $\Omega_m = 0.3$, $\Omega_\Lambda = 0.7$, and a Hubble constant $H_0 = 70$ km s^{-1} Mpc^{-1}, which implies a linear scale of 27.98 kpc arcmin^{-1} at Coma's redshift $z = 0.0231$ (NED[1] data base). For the Coma cluster, we assume $r_{500} \simeq (47 \pm 1)$ arcmin $\simeq (1.315 \pm 0.028)$ Mpc and $r_{200} \simeq 1.5 r_{500}$ as in Planck Collaboration X (2013), where r_{500} and r_{200} are the radii within which the mean density of the cluster is 500 and 200 times the critical density of the Universe, respectively.

2 COMA

2.1 X-ray surface brightness

For our analysis, we used publicly available *XMM–Newton* data, namely, the data from the EPIC/MOS (European photon imaging camera/metal oxide semiconductor) detector. The data were prepared by removing background flares using the light curve of the detected events above 10 keV and renormalizing the 'blank fields' background to match the observed count rate in the 11–12 keV band (Churazov et al. 2003). The resulting background-subtracted, exposure- and vignetting-corrected *XMM–Newton* image of the Coma cluster in the 0.5–2.5 keV energy band is presented in Fig. 1 (upper row). The zoom-in view of the NGC 4839 group is shown in the right-hand panel.

For the surface brightness analysis, we extracted X-ray counts from within circular annuli, with their centre at (RA, Dec.) = (194.94458, 27.95) = (12:59:46.699, +27:57:00.00). The sector containing the NGC 4839 group was excluded. The azimuthally averaged surface brightness profile (Fig. 2) is reasonably well fit with the one-dimensional β-model (Cavaliere & Fusco-Femiano 1978):

$$I(R) = I_o \left(1 + \frac{R^2}{r_c^2} \right)^{1/2 - 3\beta} \tag{1}$$

with the core radius $r_c = 9.9$ arcmin $\simeq 277$ kpc and $\beta = 0.71$ (see also Churazov 2016). Here, R is the projected distance from the cluster centre and I_0 is the surface brightness at the centre. The best-fitting β surface brightness profile is shown in Fig. 2 by a solid black line. This model is used in the subsequent analyses. To remove the global cluster emission and highlight the surface brightness deviations from the smooth underlying model, we divide the initial X-ray image by the best-fitting spherically symmetric β-model. The result is shown in the middle row of Fig. 1. In addition to the extended X-ray emission associated with the NGC 4839 group, there is a prominent X-ray excess (relative to the best-fitting β-model) in the west, elongated in the north–south direction, and a filamentary shaped excess (though not very prominent in this image) to the east of the Coma centre, elongated in the east–west direction (Vikhlinin et al. 1997). These substructures are also described in Neumann et al. (2003).

2.2 Temperature map

Projected temperature maps can be generated by extracting spectra from regions with a sufficient number of photon counts and then approximating them with a model of optically thin plasma. In lieu of the direct fitting procedure, we used a technique described in
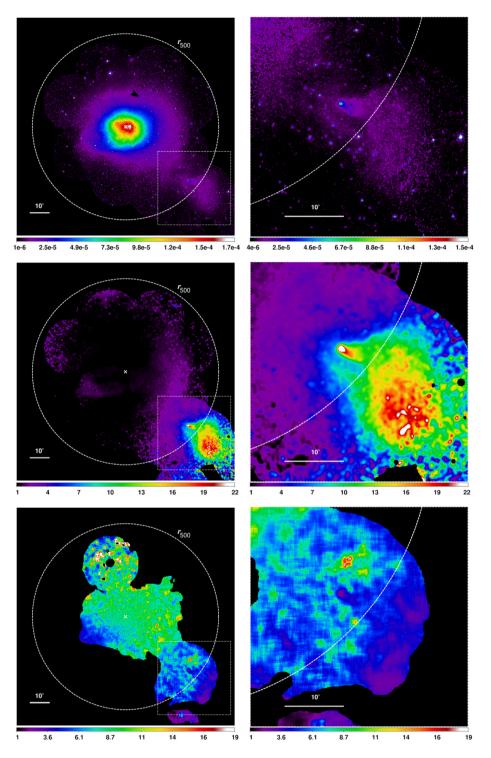
---

[1] https://ned.ipac.caltech.edu.

Figure 1. *Upper row:* XMM–Newton image of the Coma Cluster (left-hand panel) and the NGC 4839 group (right-hand panel) in the 0.5–2.5 keV energy band. *Middle row:* Surface brightness image divided by the best-fitting β-model. *Bottom row:* Projected temperature map. The white dashed circle marks the radius of $r_{500} = 47$ arcmin (Planck Collaboration X 2013). The white scale bar indicates 10 arcmin.

Churazov et al. (1996, 2016) to construct a projected temperature map of the Coma cluster. The method is computationally fast, since direct fitting is replaced by fitting two linear coefficients in the spectral model

$$\epsilon(E, T) \approx a_1 \epsilon(E, T_1) + a_2 \epsilon(E, T_2), \qquad (2)$$

where T_1 and T_2 are the (preset) temperature values which bracket the expected range of temperature variations in a given cluster and a_1 and a_2 are the two free parameters of the model. Reference models $\epsilon(E, T_1)$ and $\epsilon(E, T_2)$ are generated using the Astrophysical Plasma Emission Code (APEC) (Smith et al. 2001), fixing the Galactic hydrogen column density to $N_H = 9 \times 10^{19}$ cm^{-2} (Dickey & Lockman 1990; Kalberla et al. 2005). Once the maps of a_1 and

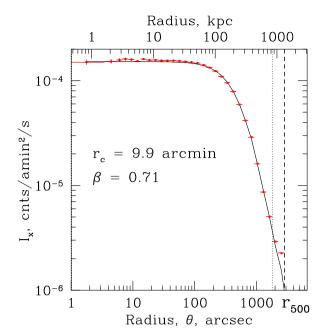**Figure 2.** Radial X-ray surface brightness profile of the Coma cluster based on the *XMM–Newton* data. The solid line shows the best-fitting β-model with core radius $r_c = 9.9$ arcmin $\simeq 277$ kpc and $\beta = 0.71$. The sector containing NGC 4839 was excluded. The dashed vertical line marks r_{500} and the dotted line shows the outer bound of the radial range used for fitting.

a_2 are generated, they can be (adaptively) smoothed and combined to determine the value of the temperature, which in the simplest form is

$$T = \frac{a_1 T_1 + a_2 T_2}{a_1 + a_2}. \qquad (3)$$

Details and a more accurate expression for the temperature are given in Churazov et al. (1996). Despite the simplicity of the method, the derived values of temperature show good agreement with the results of direct spectral fitting of individual regions. We present the (projected) temperature map of the Coma cluster derived from *XMM–Newton* data using this approach in the bottom row of Fig. 1. Each value of the temperature was calculated using adaptively chosen regions containing ∼3000 counts. For this number counts, the expected statistical uncertainty on the ICM temperature is ≲1 keV (see Fig. 3), although systematic uncertainties, associated with the non-X-ray background could be substantial. The bracketing temperature values are $T_1 = 4$ keV and $T_2 = 10$ keV. Point sources were removed before the analysis.

3 THE NGC 4839 GROUP

3.1 Observations and analysis

For the analysis of the NGC 4839 group, we use available archival *XMM–Newton* observations which cover the group and its vicinity. Some of the pointings – namely, 0652310201, 0652310301, 0652310501, 0652310601, and 0652311001 – were strongly affected by flares and, as a consequence, excluded from our analysis. From other observations, flares were removed by discarding all 15-s long time bins which contain more than six counts with energy above 10 keV per bin. The total effective exposure (see Table 1) of
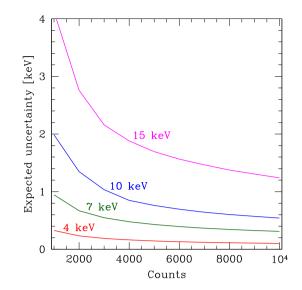
Figure 3. Pure statistical uncertainties (arising from the photon counts) of the temperature measurements for different plasma temperatures (4, 7, 10, and 15 keV) plotted against source photon counts. In the projected temperature map shown in the bottom row of Fig. 1, each value of the temperature was calculated using regions with ∼3000 photon counts.

all observations (MOS data[2]) used in the analyses in this Section is 283 ks, and for those centred on the NGC 4839 group, the exposure is 114 ks. Fig. 4 (all panels except the lower right) shows the background-subtracted, exposure- and vignetting-corrected *XMM–Newton* image in the 0.5–2.5 keV energy band. Point sources were excluded to highlight the diffuse emission SW from the core of the NGC 4839 group (tail) and towards the direction of the Coma cluster centre. Regions labelled as 'Tail' and 'Interface' (Fig. 4, upper left-hand panel) are analysed in Sections 3.1.1 and 3.1.2, regions 'inner tail', 'main tail', 'bkg', and 'Coma ICM' are discussed in Section 6.

The NGC 4839 group was also observed with the ACIS-I detector onboard the *Chandra* X-ray observatory in very faint (VFAINT) mode (ObsID 12887), with a total exposure time of 43 ks. The initial data processing is done using the recent calibration data and following the procedure described in Vikhlinin et al. (2005). This includes filtering of high background periods, application of the calibration corrections to the detected X-ray photons, and determination of the background intensity in each observation. The right-hand panel of Fig. 4 shows the available *Chandra* observation of the NGC 4839 group. Since the *Chandra* observation is relatively short and covers only the core of the group and the inner tail, only *XMM–Newton* data were used for the spectral analysis.
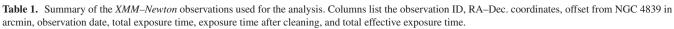
3.1.1 The tail of NGC 4839

For spectral analysis of the tail of the NGC 4839 group, we again employ the model PHABS × APEC, i.e. an absorbed single temperature thermal plasma model. We adopted the same value of the Galactic hydrogen column $N_H = 9 \times 10^{19}$ cm^{-2} as in Section 2.2. The spectral fitting is performed with XSPEC 12.9.1 (Arnaud 1996) for a set of regions labelled as 'Tail' in the top left-hand panel of Fig. 4. Fig. 5 (lower panel) shows the resulting

---

[2]Since we are looking at low surface brightness regions, we restrict ourselves to MOS data with a lower and more stable background compared to PN data.

Table 1. Summary of the *XMM–Newton* observations used for the analysis. Columns list the observation ID, RA–Dec. coordinates, offset from NGC 4839 in arcmin, observation date, total exposure time, exposure time after cleaning, and total effective exposure time.

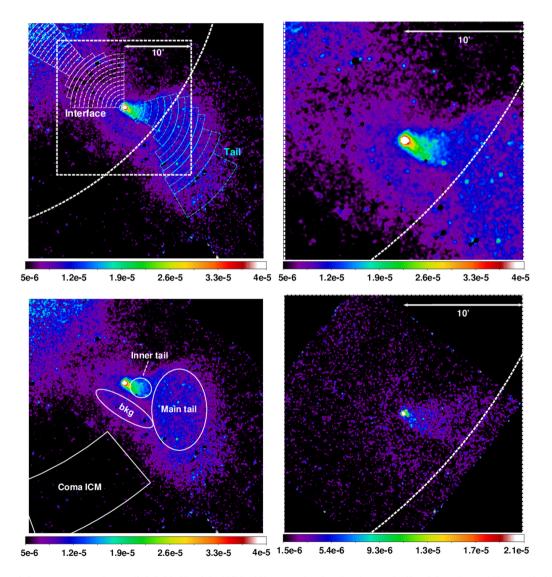| Obs ID	RA	Dec.	Offset (arcmin)	Observation date	Total duration (s)	Flare-filtered time (s)	Total eff. exposure
0652310401	$12^h57^m24^s29$	$+27°29'52''0$	0.0138	2010-06-24	23853	14325	
0652310701	$12^h57^m24^s29$	$+27°29'52''0$	0.0138	2010-06-16	21839	10050	
0652310801	$12^h57^m24^s29$	$+27°29'52''0$	0.0138	2010-12-03	16915	9187.5	
0652310901	$12^h57^m24^s29$	$+27°29'52''0$	0.0138	2010-12-05	16919	11257.5	114.2 ks
0691610201	$12^h57^m24^s65$	$+27°29'42''7$	0.1710	2012-06-02	37919	37327.5	
0691610301	$12^h57^m24^s65$	$+27°29'42''7$	0.1710	2012-06-04	35916	32092.5	
0124710101	$12^h56^m47^s68$	$+27°24'07''0$	9.9641	2000-06-21	41505	34687.5	
0124710301	$12^h58^m32^s19$	$+27°24'12''0$	16.0817	2000-06-27	28616	18375	
0124712201	$12^h57^m42^s51$	$+27°43'38''0$	14.3396	2000-12-09	27592	26737.5	168.6 ks
0403150101	$12^h57^m42^s51$	$+27°19'09''7$	11.4405	2006-06-14	54415	43725	
0403150201	$12^h57^m42^s51$	$+27°19'09''7$	11.4405	2006-06-11	55212	45052.5	
Total					360.7 ks	282.8 ks	

Figure 4. *Upper left: XMM–Newton* image (0.5–2.5 keV) of the NGC 4839 group showing the elongated tail and the enhanced X-ray emission towards the direction of the Coma cluster (north-east of the NGC 4839 nucleus). Point sources were excluded. The dashed circle marks r_{500}. The annular sectors are used in the analysis discussed in Sections 3.1.1 and 3.1.2. *Upper right:* The zoom-in view of the rectangular region marked with a white box (20×20 arcmin^2) in the left-hand panel. The white scale bar indicates 10 arcmin. *Bottom left:* The same image as in the upper panel, but showing regions discussed in Section 6. *Bottom right: Chandra* image (0.5–2.5 keV) covering the same region as in the upper right-hand panel.
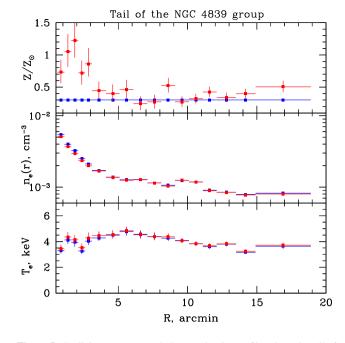
Figure 5. Radial temperature and electron density profiles along the tail of the NGC 4839 group (see regions in Fig. 4, upper left-hand panel). In blue, we show the results of spectral fitting with the ICM abundance fixed at 0.3 solar, while the case with varying gas metallicity is shown in red.
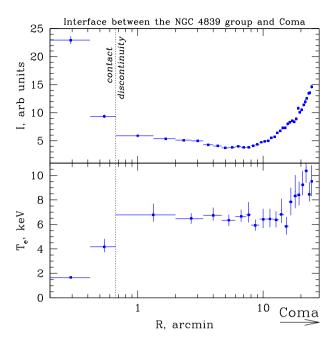

Figure 6. 'Interface' region between the NGC 4839 group and the Coma cluster. The profiles are centred on NGC 4839 (see Fig. 4, upper left) with small radii ($\lesssim 1$ arcmin) lying in the core of the group and larger radii ($\gtrsim 7$–8 arcmin) corresponding to the main Coma cluster. Surface brightness and temperature profiles result from the spectral fitting of an absorbed single-temperature thermal plasma model (phabs × apec). The exact regions are labelled as 'interface' in Fig. 4 (upper left-hand panel).

projected temperature profiles with the gas metallicity[3] fixed at 0.3 solar (Simionescu et al. 2013) and for a varying abundance. The tail of the group extends behind NGC 4839 out to $\simeq 600$ kpc and its (projected) temperature is essentially flat at $\simeq 4$ keV (consistent within the uncertainties with the results of Akamatsu et al. 2013 and Sasaki et al. 2016). The middle panel of Fig. 5 shows the electron density profile obtained from the normalization K of the APEC model:

$$K = \frac{10^{-14} n_e n_H \delta V}{4\pi (D_A (1+z))^2},\tag{4}$$

where D_A is the angular diameter distance to the Coma cluster, $z = 0.0231$ is Coma's redshift, n_e and $n_H \simeq n_e/1.2$ (for fully ionized plasma) are the mean electron and hydrogen number densities, respectively, and δV is the volume of the spectrum extraction region. We approximate the tail as a set of conic sections and assume that the size of each section along the line of sight (LOS) is equal to its transverse dimension. The gas mass density is $\rho_{gas} = \mu m_p (n_e + n_H)$ with $\mu = 0.61$ being the mean molecular weight; and the gas mass of the tail $M_{gas,tail} = \int \rho_{gas} dV \simeq 1 \times 10^{12} \, M_\odot$. While statistical uncertainties in the gas mass are small ($\simeq 0.1 \times 10^{12} \, M_\odot$), the uncertainty associated with the geometry and size of the tail could change the gas mass estimate by a factor of ~ 2. The derived $M_{gas,tail}$ agrees well with that based on *Suzaku* data (Sasaki et al. 2016): $M_{gas,tail} \simeq (0.96 \pm 0.03) \times 10^{12} \, M_\odot$.

3.1.2 Interface between Coma and the NGC 4839 group

As mentioned in the introduction, Colless & Dunn (1996) argued that the merger axis lies almost in the plane of the sky ($\alpha \simeq 75°$) with a velocity of 1700 km s^{-1} which corresponds to a Mach number $M = 1.5$ for the ambient gas temperature ~ 5 keV. In this scenario,

one expects a bow shock to form ahead of the infalling group. From the Rankine–Hugoniot jump conditions (Landau & Lifshitz 1987), the expected density and temperature jumps can be expressed as a function of the Mach number:

$$\frac{\rho_2}{\rho_1} = \frac{\mathcal{M}^2 (\gamma + 1)}{2 + \mathcal{M}^2 (\gamma - 1)},\tag{5}$$

$$\frac{T_2}{T_1} = \frac{[(\gamma - 1)\mathcal{M}^2 + 2][2\gamma \mathcal{M}^2 - (\gamma - 1)]}{(\gamma + 1)^2 \mathcal{M}^2}.\tag{6}$$

For a Mach number $M \simeq 1.5$ and $\gamma = 5/3$, the expected density jump is $\rho_2/\rho_1 \simeq 1.7$ and the expected temperature jump is $T_2/T_1 \simeq 1.5$. From the X-ray images (see Fig. 4), it is tempting to associate a 'sheath' region (the region of enhanced X-ray surface brightness between the NGC 4839 core and Coma) with the shocked gas. The edge of the 'sheath' region is located $R \sim 3$–4 arcmin away from the group centre. At these radii the projected temperature is $T \sim 6$ keV. To test this hypothesis, we extracted spectra for the set of regions shown in Fig. 4 (top left) and labelled as 'Interface'. Fig. 6 shows the surface brightness (APEC normalization) and projected temperature profiles. A steep decline of the surface brightness and a steep temperature increase at small distances ($R \lesssim 1$ arcmin) from the NGC 4839 core clearly correspond to a cold front (a contact discontinuity, separating cold gas in the core from the hotter ambient ICM). Beyond this contact discontinuity, the surface brightness demonstrates a gradual decline (at $R \simeq 1.5$–8 arcmin) and a subsequent increase (at $R \gtrsim 8$ arcmin). While the latter is clearly associated with the Coma ICM, the nature of the former is unclear, since we do not see clear signatures of a shock in the data shown in Fig. 6. We return to this question in the next sections, where we run a series of numerical simulations to

---

[3]Relative to the solar values of Lodders (2003).

Table 2. Merger parameters of SPH simulations.

ID	M_{200} $(10^{15}\,M_\odot)$	ξ	V_0 $(\mathrm{km\,s^{-1}})$	P_0 (kpc)
R10V500P2000	1.2	10	500	2000
R10V1000P4000	1.2	10	1000	4000
R60V500P2000	1.2	60	500	2000
R60V1000P3000	1.2	60	1000	3000

explain the observed profiles and to place constraints on the merger scenarios.

4 SIMULATION METHODS

We performed SPH simulations to investigate the merging scenario of NGC 4839 group by using the GADGET-2 code (Springel, Yoshida & White 2001). To simplify the merger process, we only consider the interaction between a main cluster and an infalling subcluster. Each body is further modelled as a spherical object consisting of a dark matter (DM) halo and gas atmosphere. A detailed description of the simulation method has been given in Zhang, Yu & Lu (2014, 2015). Here, we only provide a brief summary.

(i) The merging process is modelled in Cartesian coordinates (x, y, z). The centre of mass of the merging system is initially set at rest at the origin of the coordinates. The merger plane coincides with the x–y plane. The DM haloes and gas haloes follow the NFW profile (Navarro, Frenk & White 1997) and the Burkert profile (Burkert 1995) within the virial radius for the density profiles (see equations 1–4 in Zhang et al. 2014). We fix the masses of haloes as described below and set the concentration parameter of the main cluster $c = 4$ according to the weak-lensing measurement (Okabe et al. 2014). The concentration parameter of the subcluster, however, is determined from the mass–concentration relation of Duffy et al. (2008).

(ii) The merger configuration between two clusters is described by the following four parameters: the virial mass of the main cluster M_{200}, the mass ratio between the main cluster and the subcluster ξ (> 1), the initial relative velocity V_0, and the impact parameter P_0. Motivated by recent weak-lensing studies (Okabe et al. 2014), we fix the Coma cluster mass at $M_0 = 1.2 \times 10^{15}\,M_\odot$ in all our simulations, but vary the other three parameters to find a 'best-fitting' model for NGC 4839 (see Table 2 for the parameter settings used in the simulations). We consider two different values for the mass ratio between Coma and the NGC 4839 group: $\xi = 10$ and 60. The former corresponds to the mass ratio estimate of Colless & Dunn (1996), and the latter is motivated by the gas mass estimate obtained in Section 3.1.1: if we assume the baryon fraction of ~10 per cent, then the total mass of the NGC 4839 group is ~$10^{13}\,M_\odot$. We return to the question of the mass ratios below.

We stress here that, we do not intend to find an exact match between our simulations and observations in this study, but rather to understand the possible merger scenario(s). That is the reason why we did not survey a large parameter space, but test a few specified merger cases with large/small mass ratios and high/low initial angular momentum. We also only present the simulation results while assuming the LOS is parallel to the z-axis, since, as mentioned above, available estimates of the viewing angle (Colless & Dunn 1996) favour a plane of the sky merger. Moreover, if the group is on its first radial infall into the Coma cluster, as it is widely assumed,

the group is expected to move supersonically with an infall velocity of ~2000 km s^{-1}. The LOS velocity of the NGC 4839 group relative to the Coma cluster is only $V_r \simeq 470$ km s^{-1} (Adami et al. 2005), i.e. much smaller compared to the local speed of sound. Thus, to reconcile the measured LOS velocity with the first radial infall, the viewing angle should be close to $90°$.

5 RESULTS

We discuss two possible merger scenarios for the NGC 4839 group in this section, including (1) the group is in the pre-merger stage (i.e. before the primary pericentric passage[4]); (2) the group is near the primary apocenter. We show that our SPH simulations favour the latter scenario, but the former one still cannot be definitely excluded.

5.1 Pre-merger scenario

Fig. 7 (top and middle panels) shows the X-ray surface brightness distribution in the runs R60V500P2000 and R60V1000P3000 at $t = -0.5$ Gyr, where the dashed line shows the trajectory of the infalling subcluster throughout the simulation. In this image, we see a straight gaseous tail trailing the subcluster. The subcluster, however, still retains most of the gas in its gravitational potential well, because it has not yet entered the high gas density region in the main cluster. Therefore, in this scenario, the gas mass of the tail ~$10^{12}\,M_\odot$ (see Section 3.1.1) can be used to estimate the total mass of the group $M_{200} \sim 10^{13}\,M_\odot$, assuming a gas mass fraction of ~10 per cent (Vikhlinin et al. 2006; Sun et al. 2009). Fig. 7 (lower panel) shows the profiles of the X-ray surface brightness and the X-ray emission weighted temperature along the line connecting the centres of the two clusters. The vertical dashed line in this panel marks the position of the shock front. Notice that the shock front itself is not prominent in the X-ray surface brightness profile. Typically, shock fronts are detected in X-ray images as surface brightness edges. Our simulations suggest that the shock front, associated with the NGC 4839 group, is actually located close to the lowest surface brightness region in the X-ray image (Fig. 7) and not in a region of surface brightness enhancement. Motivated by these results, one can expect to detect a bow shock at a distance of $\simeq 5$–6 arcmin (the lowest surface brightness region in Fig. 6) from the contact discontinuity (cold front), corresponding to the leading edge of the group. At the same time, the stand-off distance Δ, i.e. the distance between a stagnation point and the closest point on the bow shock, can be estimated from the Mach number (Moekel 1949; Farris & Russell 1994; Verigin et al. 2003; Zhang et al. 2019, among others). According to equation (35) in Verigin et al. (2003) (see also equation A4 in Zhang et al. 2019), for the NGC 4839 group, infalling radially and with a Mach number $\simeq 1.5$, the stand-off distance $\Delta \simeq 0.7 \times R_{cf}$, where $R_{cf} \simeq 1$ arcmin is the curvature radius of the cold front. Thus, we have a clear contradiction between predictions for the bow shock position. Projection effects do not play a significant role here, since, as discussed above, the merger should happen almost in the plane of the sky if the NGC 4839 group is on its first infall into Coma. So we conclude that available X-ray data and our calculations of the stand-off distance disfavour the pre-merger stage.

Moreover, since the stripped gas is distributed mostly along the trajectory of the infalling subcluster before the core passage, runs

---

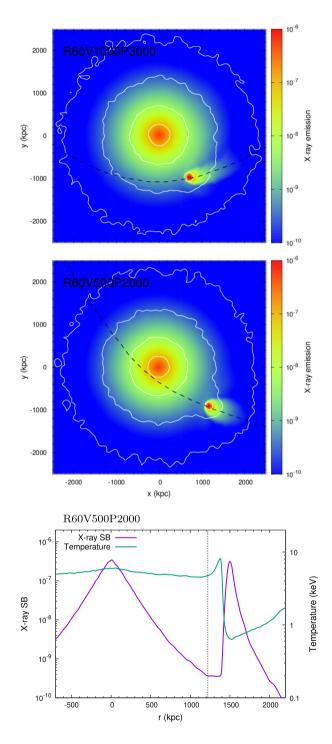[4]For convenience, we set the evolution time $t = 0$ at the moment of primary pericentric passage.

R60V500P2000 and R60V1000P3000 show different tail directions relative to the centre of the main cluster if the LOS is perpendicular to the merger plane (see Fig. 7). These two runs have different initial angular momenta. In practice, however, there is a degeneracy while determining the angular momentum of the subcluster and the viewing angle from the *Chandra/XMM–Newton* X-ray images (the wake of NGC 4839 is nearly parallel to the radial direction of Coma in the sky plane). In spite of this, tails of the subclusters remain almost straight and symmetric in both runs, because there is no sharp turn in their motion (it only occurs near the apocenter when the merging system has a relatively small initial angular momentum, see Section 5.2 for more discussion). This is obviously different from what we observe in NGC 4839. In this regard, our simulations disfavour the pre-merger scenario. However, we stress that it is still possible to explain the observed 'wiggling' tail as a result of von Kármán vortex shedding, which generally occurs behind a moving blunt body with a Reynolds number $\gtrsim 100$ (e.g. Williamson 1996). The onset of vortex shedding, however, is usually delayed in numerical simulations since numerical viscosity suppresses growth of the instabilities (Braza, Chassaing & Ha 1986). We simply estimate the vortex shedding period T_{vortex} of the wake if assuming the Strouhal number $\mathrm{St} = D/T_{\mathrm{vortex}}U \simeq 0.2$, where U ($\sim 2000\,\mathrm{km\,s^{-1}}$) and D ($\sim 200\,\mathrm{kpc}$) are the velocity and size of the infalling cluster in the simulation. The period $T_{\mathrm{vortex}} \sim 0.5\,\mathrm{Gyr}$ is thus shorter than (or comparable to) the crossing time (size of the subcluster divided by the velocity of an oncoming stream of the surrounding gas) of the subcluster.

5.2 Post-merger scenario

Fig. 8 shows the time evolution of the X-ray surface brightness and X-ray weighted temperature distributions in the run R10V500P2000. The panels illustrate four different merger stages, i.e. (1) pre-merger, (2) post-pericentric passage, (3) apocentric passage, and (4) secondary core accretion (from left to right). The simulated image shown in Fig. 8 panel (3a) (apocentric passage) resembles the observed X-ray morphology (see Figs 1 and 4). Our simulation provides a good match with the real X-ray observations (compare panel 3a in Fig. 8 with the upper panel of Fig. 1), when the subcluster is close to, but shortly after, the primary apocentric passage. The subcluster trails a large and asymmetric tail, whose formation could be understood in the following way:

(i) During the pericentric passage, the gas in the NGC 4839 group is driven by the ram pressure and forms a tail trailing the galaxy.

(ii) When the subcluster approaches apocenter, it slows and reverses its radial velocity.

(iii) At the same time, the ram pressure decreases and the subcluster gas falls into the local gravitational potential well of the group.

(iv) Shortly after the apocenter passage, the DM, stars, and the gaseous core are moving towards the Coma cluster centre, while the displaced gas moves in the opposite direction, forming the structure as in the panel (3a) of Fig. 8.

The last two stages are illustrated in Fig. 9 showing the flow patterns in and around the infalling group. As argued above, this structure is formed when the subcluster is turning sharply. This is the reason why the run R10V500P2000 gives a better match with the observations than R10V1000P4000 (the infalling subcluster holds larger angular momentum in this run). For the large impact parameter (R10V1000P4000), there is no strong interaction between the infalling group and the main cluster. After pericentric
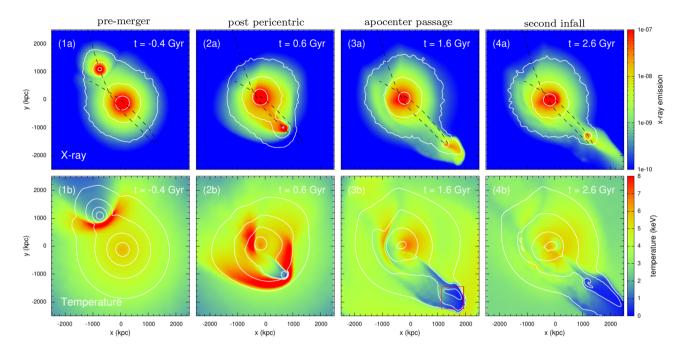

Figure 7. *Upper and middle panels:* X-ray surface brightness distribution of the runs R60V1000P3000 and R60V500P2000 at $t = -0.5\,\mathrm{Gyr}$. The white contours show the distribution of the mass surface density. The black dashed curves reveal the trajectory of the infalling subcluster. *Lower panel:* profiles of the X-ray surface brightness and X-ray emission weighted temperature (for R60V500P2000) along the line connecting the centres of the two merging subclusters. The horizontal axis represents the distance from the centre of the main cluster. Note that the tail is symmetric and the bow shock is not prominent in the X-ray surface brightness map/profile and is actually located in the region of minimal surface brightness (for details see the text).

Figure 8. Time evolution of the X-ray surface brightness (top row) and X-ray weighted temperature (bottom row) distributions of the run R10V500P2000. These panels illustrate four stages of the merger process (from left to right): pre-merger, post-pericentric passage, apocentric passage, and secondary core accretion. The white contours show the mass surface density (top panels) and the X-ray surface brightness (bottom panels) distributions. The black dashed curve in the top panels shows the trajectory of the infalling subcluster with the initial infall located at the top left of the box. The gas mass belonging to the subcluster within the red box marked in panel (3b) is $M_{gas} \simeq 5 \times 10^{12} \, M_{\odot}$, broadly consistent with the gas mass estimate from the X-ray analysis. Panel (3a) provides a good match with the X-ray morphology of the NGC 4839 group, when the subcluster crosses the apocenter (compare with Fig. 1), which favours the post-merger scenario.
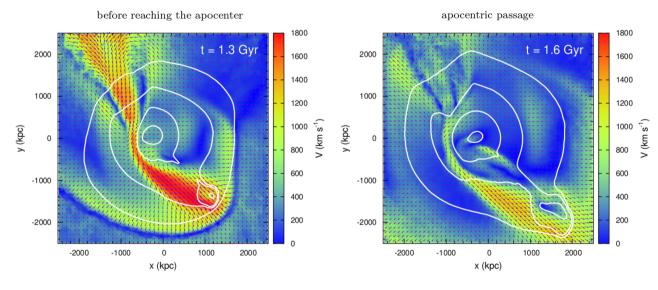

Figure 9. The slice in gas velocities (taken in the merger plane) for the post-merger scenario, overlapped with the X-ray surface brightness (white contours). The colourmap colour codes absolute values of velocities in the rest frame of the mass centre of the merging clusters (Coma + NGC 4839). Arrows show the velocity vectors. The *left-hand* and *right-hand* panels show the moments before and after the apocentric passage, respectively. As the NGC 4839 group approaches the apocenter (left-hand panel), it slows. The ram pressure decreases and the tail gas falls back towards the core of the group, driven by the gravitational drag from the subcluster. Just after the apocentric passage (right-hand panel), the NGC 4839 group starts its second infall into the Coma cluster core, while the gaseous tail is moving in the opposite direction (towards the south-west). The right-hand panel shows the same time as panels (3a) and (3b) in Fig. 8.

passage, the core of the subcluster remains roughly round, while X-ray data clearly show an edge-like structure at the head of the group.

Fig. 8 shows that the subcluster penetrates the central gas core of the main cluster and a large fraction of gas is stripped away from its potential well through this process. We measure the gas mass

belonging to the subcluster within the red box marked in panel (3b) (integrated over the LOS), i.e. $M_{gas} \simeq 5 \times 10^{12} \, M_{\odot}$. This result is of the same order of magnitude as the gas mass estimate obtained in Section 3.1.1. We note that the post-merger scenario requires a smaller mass ratio (i.e. higher mass of the NGC 4839 group) than
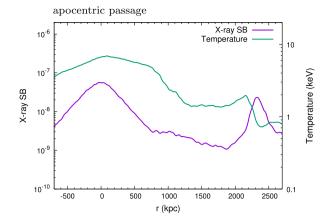
Figure 10. Same as in the bottom panel of Fig. 7, but for the post-merger scenario (R10V500P2000, $t = 1.6$ Gyr). The surface brightness and temperature profiles bear some morphological similarities with the pre-merger profiles, but the shock between the group and the main cluster is now absent. As a result, no very sharp features are seen in the profiles and the amplitude of temperature variations is markedly smaller.

that of the pre-merger scenario. Otherwise, after the primary core passage, the subcluster loses almost all its gas. In panels (1b) and (2b), prominent shock waves are driven by the infalling subcluster. However, shocks usually move faster than the subcluster after pericentric passage (Zhang et al. 2019). Thus, we do not expect to see shocks near NGC 4839. The absence of a shock is also illustrated in Fig. 10 which shows the X-ray surface brightness and X-ray emission weighted temperature for the post-merger scenario, i.e. shortly after the apocenter passage, along the line connecting the group and the main cluster. No very sharp features are seen in the profiles and the amplitude of temperature variations is markedly smaller compared to the pre-merger case shown in Fig. 7, bottom panel.

At the moment when the subcluster is near the apocenter, the bow shock associated with the first infall of NGC 4839 has propagated south-west much farther away from the core of the group and its current position is roughly consistent with the Coma radio relic (Giovannini, Feretti & Stanghellini 1991). We will discuss the origin of the Coma relic in more detail in Lyskova et al. (in preparation). The observed hot 'sheath' region, as seen in the X-ray data (see Figs 1 and 4), that surrounds the brighter NGC 4839 subcluster core, can be also explained under the post-merger scenario. If the impact parameter of the merger is not too high, then the subcluster, just after the apocenter passage, starts moving through its own tail of stripped gas (see flow patterns in Fig. 9, right-hand panel). An increased temperature and gas density in the 'sheath' region could be due to interaction of the re-infalling subcluster with the stripped gas mixed with the Coma ICM. One possible mechanism here is the 'stolen atmosphere' effect (described in Sheardown et al. 2018), when intracluster gas, surrounding the subcluster, is drawn into the NGC 4839 group potential and compressed/heated. We defer the discussion of the nature of observed 'sheath' for future work.

To check results obtained with the SPH simulations, we also ran a FLASH simulation using the same merging parameters as those used in run R10V500P2000. The simulated surface brightness and temperature maps are consistent with results of the SPH simulations. Moreover, Sheardown (2019) inspected a large set of FLASH simulations of idealized binary cluster mergers and independently reached the same conclusion that the NGC 4839

Table 3. Summary of mass estimates of the Coma cluster and the NGC 4839 group.

Object	Study	M_{200}, 10^{14} M$_\odot$
Coma	M–T, T = 8 keV	12.6
Coma	Okabe et al. (2014)	12.0
Coma	Colless & Dunn (1996)	12.9
NGC 4839	M–T, T = 4 keV	4.2
NGC 4839	M–T, T = 2.4 keV	1.9
NGC 4839	Okabe et al. (2014)	>1
NGC 4839	Colless & Dunn (1996)	0.9

group is most likely to have passed by the Coma core from the north-east with a small impact parameter and is now on its next infall.

6 DISCUSSION

6.1 Mass of the NGC 4839 group

As discussed above, the mass of the NGC 4839 group is poorly constrained. We briefly summarize here the mass and the mass ratio estimates $\xi = M_{\rm vir}(\text{Coma})/M_{\rm vir}(\text{NGC 4839})$ available in the literature. From the analysis of the velocity distributions of the cluster/group members, Colless & Dunn (1996) obtained the virial masses of $\simeq 1.3 \times 10^{15}$ and $\simeq 8.6 \times 10^{13}$ M$_\odot$ for the Coma cluster and the NGC 4839 group, respectively. So their mass ratio is $\simeq 15$.

Based on the weak-lensing signal, Okabe et al. (2014) measured the Coma virial mass of $M_{\rm vir}(\text{Coma}) = 1.2 \times 10^{15}$ M$_\odot$ and the total mass of the NGC 4839 group within the tidal (truncation) radius $M(r < 98$ kpc$) \simeq 1.6 \times 10^{13}$ M$_\odot$. This estimate was obtained assuming that the group mass density outside the truncation radius, $r_{\rm t} = 98$ kpc, is close to zero. This measurement can constrain the virial (M_{200}) mass of the NGC 4839 group, assuming that the mass profile within $r_{\rm t}$ has not been modified by the merger. We described the mass density with the NFW profile and explored a range of M_{200} and c_{200}. The weak-lensing estimate agrees reasonably well with the group virial mass of $> 1 \times 10^{14}$ M$_\odot$. The NFW mass profiles with $M_{200} \sim 10^{13}$ M$_\odot$ are in more than 3σ tension with the weak-lensing estimate. In Table 3, we provide a summary of the NGC 4839 group mass (and the mass ratio) estimates. Note that this table is not intended to cover all Coma mass measurements available in the literature.

The masses also can be estimated via X-ray scaling relations. To convert M_{500} to M_{200}, we use the following relation (obtained for the concentration parameter $c = 4$): $R_{500}/R_{200} = 0.65$ and $M_{500}/M_{200} = 5/2 \times (0.65)^3 = 0.69$. If the NGC 4839 group is characterized by 4 keV gas, then according to the M–T relation (Vikhlinin et al. 2006; Sun et al. 2009), its $M_{500} \simeq 2.9 \times 10^{14}$ M$_\odot$ and $M_{200} \simeq 4.2 \times 10^{14}$ M$_\odot$. For the Coma cluster with its 8 keV gas, the M–T relation gives $M_{200} \simeq 1.26 \times 10^{15}$ M$_\odot$. These arguments suggest that the mass ratio between the subcluster and the main cluster is $\simeq 3$. However, such a mass ratio implies a major merger scenario and is disfavoured by our simulations – in this case, the Coma cluster would be dramatically disturbed, and strong shocks, propagating to the north-east and south-west, would be generated. The best-fitting post-merger simulation with the mass ratio of $\xi \sim 10$ provides a good match to the observed morphology of the tail of the group, but the measured ratio of gas temperatures in the tail and in the main cluster do not agree well with simulations. In the simulations, the temperatures of the main cluster and the tail of the subcluster are $\simeq 5$ keV and $\simeq 0.5$–1 keV, correspondingly, i.e. the temperature ratio

Table 4. Summary of the spectral fits in different regions shown in Fig. 4, lower left-hand panel. The uncertainties are 1σ confidence level. For the fitting of a thermal plasma, we used the single-temperature (phabs $\times$ apec) model or two-temperature (phabs $\times$ (apec$_1$ + apec$_2$)) model with 464 PHA bins. Since the actual metallicity of gas in the 'inner tail' region is not known, for fitting the two-temperature model, we consider two cases: $Z = 0.5\,Z_\odot$ and $0.7\,Z_\odot$.

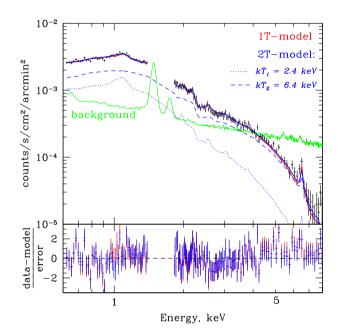| Region	K_1, 10^{-5}	kT_1, keV	Z_1 ($Z_\odot$)	K_2, 10^{-5}	kT_2, keV	Z_2 ($Z_\odot$)	χ^2/d.o.f.
'bkg'	5.12 ± 0.08	6.4 ± 0.2	$0.25^{+0.09}_{-0.08}$	–	–	–	372/461
'inner tail'	8.34 ± 0.15	$4.2^{+0.2}_{-0.1}$	0.71 ± 0.07	–	–	–	384/461
'main tail'	6.01 ± 0.03	**4.2 $\pm$ 0.1**	0.3 (fixed)	–	–	–	425/462
'inner tail'	$2.94^{+0.66}_{-0.33}$	$2.2^{+0.3}_{-0.1}$	0.5 (fixed)	$6.06^{+0.32}_{-0.67}$	6.4 (fixed)	0.25 (fixed)	387/461
'inner tail'	$4.40^{+2.08}_{-1.62}$	$3.1^{+0.8}_{-0.7}$	0.7 (fixed)	$4.27^{+1.72}_{-2.25}$	6.4 (fixed)	0.25 (fixed)	379/461
'main tail'	$2.27^{+0.33}_{-0.30}$	**2.4 $\pm$ 0.3**	0.3 (fixed)	$3.84^{+0.30}_{-0.33}$	6.4 (fixed)	0.25 (fixed)	407/461

Figure 11. The observed spectrum (black crosses) of the 'main tail' region and the best-fitting models. The single-temperature thermal plasma model is shown in red. The best-fitting gas temperature is 4.2 ± 0.1 keV (see Table 4). A similar quality fit can be obtained with a two-temperature model (blue solid line). In this model, the first component (blue dotted line) is due to the group gas, while the second component (blue dashed line) represents the LOS contribution of the Coma cluster ICM mixed with the stripped group gas. The temperature and abundance of the second component are fixed at the values obtained for the 'bkg' region (see Fig. 4, lower left-hand panel), viz., $kT = 6.4$ keV and $Z = 0.25\,Z_\odot$ (see Table 4). The best-fitting temperature of the tail gas decreases to 2.4 ± 0.3 keV. The green line shows the background from blank fields to which an additional component (representing a variable particle background in these particular observations) is added. Both the single- and two-temperature models fit the spectrum reasonably well (see Table 4). It is therefore plausible that the characteristic temperature of the NGC 4389 gas is $\sim$2 keV, implying a lower initial mass of the group.

is $\sim$5–10. However, the observed ratio of the X-ray temperatures $\simeq$8 keV/4 keV = 2 is noticeably different. As a consequence, the mass ratio derived from the M–T relation is several times smaller than in simulations.

6.2 Temperature of the NGC 4839 group

The projected spectra analysed in Section 3 have not been corrected for the additional contribution that might come from the Coma gas along the LOS but outside the volume occupied by the tail.

This was motivated by the much higher surface brightness of the tail region compared to the typical Coma brightness at the same distance (see the upper panel of Fig. 1). Even if we redo our spectral analysis using the 'Coma ICM' region (see Fig. 4, lower left-hand panel) as a background, the main conclusions remain unchanged. However, according to Fig. 4, the NGC 4839 group seems to coincide with some surface brightness enhancement. For the post-merger scenario, the observed tail is formed when the core of the group turns sharply at the apocenter. So the overall surface brightness enhancement, which was previously thought to be shocked gas (e.g. Neumann et al. 2001), in our simulations is actually group gas, stripped before the apocenter passage, and partly mixed with Coma gas. To account for its contribution to the observed spectra, we treat the region adjacent to the core of the group (marked as 'bkg' in Fig. 4, lower left-hand panel) as the actual background. We extract and fit the 'bkg' spectrum with an absorbed single-temperature thermal plasma model. Results are provided in Table 4. We model the 'main tail' (see Fig. 4, lower left-hand panel) spectrum with two APEC components. One component is for the 'background' gas, the other is for the tail gas. We fix the temperature and the abundance of the 'background' gas at best-fitting values from the previous step (see Table 4) and vary its normalization along with parameters of the APEC model representing the tail gas. Since the 3D geometry of the merger is poorly known, we allow the background normalization to vary by a factor of $\sim$2 relative to the best-fitting values for the single-temperature fit. As a result, for the two-temperature model, the 'main tail' temperature decreases to $\simeq$ 2.4 keV. Note that both the single- (two free parameters) and the two-temperature (three free parameters) models provide an adequate fit to the data (Fig. 11). While the modest residuals seen in the bottom panel of Fig. 11 suggest that the spectrum is more complicated than our model, the main point we want to emphasize is that the two-temperature model fit with the temperature of one component fixed at 6.4 keV, produces very reasonable normalizations of two components, consistent with an assumption of a cool 2.4 keV group gas embedded into a hotter ICM of the main cluster mixed with the outer layers of the tail. We analysed also the 'inner tail' region (see Fig. 4, lower left-hand panel) in a similar way. The temperature of the inner tail is found to be $\simeq$ 2.2 keV, if we assume that the abundance of heavy elements is $0.5\,Z_\odot$. A higher metallicity gives higher temperature and larger uncertainties (see Table 4). If the tail temperature is indeed 2.4 keV, then the NGC 4839 group mass is $M_{200} \simeq 1.9 \times 10^{14}\,M_\odot$ from the M–T relation, and the mass ratio between Coma and the group is $\simeq$6.6. While this does not resolve the discrepancy between observations and simulations completely, it certainly reduces the tension.

To some extent the tension between the mass/temperature ratios in simulations and observations also could be weakened if one finds

the best-fitting configuration of the merger that exactly matches all available observations, but this task is beyond the scope of our paper.

7 CONCLUSIONS

Coma, as one of the nearest massive galaxy clusters, provides a unique close-up view of ongoing mergers. One of the most striking merger events involves the NGC 4839 group which lies in the Coma cluster outskirts (∼1 Mpc in projection) in the south-west direction from the cluster centre. The X-ray images of the subcluster exhibit a cold front at the head of the group, a 'sheath' region of hotter gas enveloping the core of the group, and an elongated tail of ram pressure stripped gas toward the south-west, i.e. the opposite direction of the Coma cluster centre. We discuss two possible scenarios of the merger: (1) the group is on its first infall before the primary pericentric passage, and (2) the group is near the primary apocenter. The data and simulations favour the latter scenario in agreement with the earlier suggestion by Burns et al. (1994).

    (i) Pre-merger scenario

In the first scenario, the NGC 4839 group comes from the south-west along the filament connecting Coma with Abell 1367 and it has just started to penetrate the Coma ICM, then the group is expected to move supersonically with Mach number ≳1.5. The position of the bow shock, predicted by our simulations, corresponds to a surface brightness minimum along the line connecting the two merging subclusters, while customarily shock fronts are identified with a sharp increase of the surface brightness. However, the expected position of a bow shock cannot be reconciled with the stand-off distance estimate. Thus, we conclude that we do not see a strong shock. We also showed that if the group is on its first radial infall, then the merger is most likely to be almost in the plane of the sky, i.e. non-detection of the shock cannot be attributed to projection effects. Moreover, the pre-merger simulations do not reproduce the observed X-ray appearance of the tail of the NGC 4839 group. In simulations, tails remain almost straight and symmetric, while the observed morphology is more complex. So we conclude, our analysis disfavours the radial infall scenario.

    (ii) Post-merger scenario

In the post-merger scenario, a good match between the modelling and the real X-ray observations is achieved when the infalling group has just passed apocenter. Under this scenario, the observed morphology of the tail is formed in the following way. When the subcluster approaches the apocenter, it slows and then reverses its direction of motion. At the same time, the ram pressure ceases and the group gas falls back into the local potential well of the group, overshooting an equilibrium position and appearing on the other side of the group core. Shortly after apocenter passage, the core of the subcluster starts moving towards the Coma cluster centre, while the displaced gas moves in the opposite direction. The observed 'sheath' – a region of slightly denser and hotter gas than the ambient gas in front of the group – could arise due to interaction of the subcluster, now moving back towards the Coma centre, with its own tail gas now mixed with the gas of the main cluster. In the post-merger scenario, we do not expect shocks near NGC 4839 since the bow shock associated with the first infall of the group has already propagated towards the south-west, much farther away from the group. The current position of the shock is roughly consistent with the Coma radio relic.

REFERENCES

Adami C., Biviano A., Durret F., Mazure A., 2005, A&A, 443, 17
Akamatsu H., Inoue S., Sato T., Matsusita K., Ishisaki Y., Sarazin C. L., 2013, PASJ, 65, 89
Andrade-Santos F., Nulsen P. E. J., Kraft R. P., Forman W. R., Jones C., Churazov E., Vikhlinin A., 2013, ApJ, 766, 107
Arnaud K. A., 1996, in Jacoby G. H., Barnes J., eds, ASP Conf. Ser. Vol. 101, Astronomical Data Analysis Software and Systems. Astron. Soc. Pac., San Francisco, p. 17
Berrier J. C., Stewart K. R., Bullock J. S., Purcell C. W., Barton E. J., Wechsler R. H., 2009, ApJ, 690, 1292
Biviano A., Durret F., Gerbal D., Le Fevre O., Lobo C., Mazure A., Slezak E., 1996, A&A, 311, 95
Bonafede A., Giovannini G., Feretti L., Govoni F., Murgia M., 2009, A&A, 494, 429
Braza M., Chassaing P., Ha M., 1986, J. Fluid Mech., 165, 79
Briel U. G. et al., 2001, A&A, 365, L60
Brown S., Rudnick L., 2011, MNRAS, 412, 2
Burkert A., 1995, ApJ, 447, L25
Burns J. O., Roettiger K., Ledlow M., Klypin A., 1994, ApJ, 427, L87
Cavaliere A., Fusco-Femiano R., 1978, A&A, 70, 677
Churazov E., Gilfanov M., Forman W., Jones C., 1996, ApJ, 471, 673
Churazov E., Forman W., Jones C., Böhringer H., 2003, ApJ, 590, 225
Churazov E. et al., 2012, MNRAS, 421, 1123
Churazov E., Arevalo P., Forman W., Jones C., Schekochihin A., Vikhlinin A., Zhuravleva I., 2016, MNRAS, 463, 1057
Colless M., Dunn A. M., 1996, ApJ, 458, 435
Di Gennaro G. et al., 2018, ApJ, 865, 24
Dickey J. M., Lockman F. J., 1990, ARA&A, 28, 215
Dolag K., Borgani S., Murante G., Springel V., 2009, MNRAS, 399, 497
Duffy A. R., Schaye J., Kay S. T., Dalla Vecchia C., 2008, MNRAS, 390, L64
Ensslin T. A., Biermann P. L., Klein U., Kohle S., 1998, A&A, 332, 395
Erler J., Basu K., Trasatti M., Klein U., Bertoldi F., 2015, MNRAS, 447, 2497
Farris M. H., Russell C. T., 1994, J. Geophys. Res., 99, 17681
Geller M. J., Huchra J. P., 1989, Science, 246, 897
Genel S., Bouché N., Naab T., Sternberg A., Genzel R., 2010, ApJ, 719, 229

Giovannini G., Feretti L., Stanghellini C., 1991, A&A, 252, 528

Kalberla P. M. W., Burton W. B., Hartmann D., Arnal E. M., Bajaja E., Morras R., Pöppel W. G. L., 2005, A&A, 440, 775

Kravtsov A. V., Borgani S., 2012, ARA&A, 50, 353

Landau L. D., Lifshitz E. M., 1987, Fluid Mechanics, Vol. 6, 2nd edn. Butterworth-Heinemann, UK

Lodders K., 2003, ApJ, 591, 1220

Markevitch M., Vikhlinin A., 2007, Phys. Rep., 443, 1

Moeckel W. E., 1949, Approximate Method for Predicting Form and Location of Detached Shock Waves Ahead of Plane or Axially Symmetric Bodies, NACA Technical Note 1921. National Advisory Comittee for Aeronautics. Lewis Flight Propulsion Lab, Cleveland, Ohio, USA

Navarro J. F., Frenk C. S., White S. D. M., 1997, ApJ, 490, 493

Neumann D. M. et al., 2001, A&A, 365, L74

Neumann D. M., Lumb D. H., Pratt G. W., Briel U. G., 2003, A&A, 400, 811

Ogrean G. A., Brüggen M., 2013, MNRAS, 433, 1701

Okabe N. et al., 2014, PASJ, 66, 99

Planck Collaboration X, 2013, A&A, 554, A140

Roediger E. et al., 2015a, ApJ, 806, 103

Roediger E. et al., 2015b, ApJ, 806, 104

Sasaki T., Matsushita K., Sato K., Okabe N., 2016, PASJ, 68, 85

Sheardown A. et al., 2018, ApJ, 865, 118

Sheardown A. et al., 2019, preprint (arXiv:1903.00482)

Simionescu A. et al., 2013, ApJ, 775, 4

Smith R. K., Brickhouse N. S., Liedahl D. A., Raymond J. C., 2001, ApJ, 556, L91

Springel V., Yoshida N., White S. D. M., 2001, New Astron., 6, 79

Su Y. et al., 2017, ApJ, 835, 19

Sun M., Jones C., Forman W., Nulsen P. E. J., Donahue M., Voit G. M., 2006, ApJ, 637, L81

Sun M., Voit G. M., Donahue M., Jones C., Forman W., Vikhlinin A., 2009, ApJ, 693, 1142

Sun M., Donahue M., Roediger E., Nulsen P. E. J., Voit G. M., Sarazin C., Forman W., Jones C., 2010, ApJ, 708, 946

van Weeren R. J., Röttgering H. J. A., Brüggen M., Cohen A., 2009, A&A, 505, 991

van Weeren R. J., Röttgering H. J. A., Brüggen M., Hoeft M., 2010, Science, 330, 347

Verigin M. et al., 2003, J. Geophys. Res., 108, 1323

Vikhlinin A., Forman W., Jones C., 1997, ApJ, 474, L7

Vikhlinin A., Markevitch M., Murray S. S., Jones C., Forman W., Van Speybroeck L., 2005, ApJ, 628, 655

Vikhlinin A., Kravtsov A., Forman W., Jones C., Markevitch M., Murray S. S., Van Speybroeck L., 2006, ApJ, 640, 691

Vikhlinin A. A., Kravtsov A. V., Markevich M. L., Sunyaev R. A., Churazov E. M., 2014, Phys.-Usp., 57, 317

Williamson C. H. K., 1996, Annu. Rev. Fluid Mech., 28, 477

Zhang C., Yu Q., Lu Y., 2014, ApJ, 796, 138

Zhang C., Yu Q., Lu Y., 2015, ApJ, 813, 129

Zhang C., Churazov E., Forman W. R., Jones C., 2019, MNRAS, 482, 20

This paper has been typeset from a TeX/LaTeX file prepared by the author.